

## RESEARCH ARTICLE

# Extrusion bioprinting of elastin-containing bioactive double-network tough hydrogels for complex elastic tissue regeneration

Di Wang<sup>1</sup>  | Jinshi Zeng<sup>1</sup> | Hailin Zhu<sup>2</sup> | Siyu Liu<sup>1</sup> | Litao Jia<sup>1</sup> | Wenshuai Liu<sup>1</sup> | Qian Wang<sup>1</sup> | Senmao Wang<sup>1</sup> | Wei Liu<sup>1</sup> | Jiayu Zhou<sup>1</sup> | Huimin Chen<sup>2</sup> | Xia Liu<sup>1</sup> | Haiyue Jiang<sup>1</sup> 

<sup>1</sup>Plastic Surgery Hospital of Chinese Academy of Medical Sciences & Peking Union Medical College, Beijing, P.R. China

<sup>2</sup>SinoBioprint Biotech Ltd., Shanghai, P.R. China

## Correspondence

Haiyue Jiang and Xia Liu, Plastic Surgery Hospital of Chinese Academy of Medical Sciences & Peking Union Medical College, Beijing 100144, P.R. China.

Email: [jianghaiyue@psh.pumc.edu.cn](mailto:jianghaiyue@psh.pumc.edu.cn) and [liuxia@psh.pumc.edu.cn](mailto:liuxia@psh.pumc.edu.cn)

## Funding information

Chinese Academy of Medical Sciences Innovation Fund for Medical Sciences, Grant/Award Numbers: 2021-I2M-1-052, 2017-I2M-1-007; National Multidisciplinary Cooperative Diagnosis and Treatment Capacity Building Project for Major Diseases, Grant/Award Number: 21025; National Natural Science Foundation of China, Grant/Award Numbers: 82371796, 81871575

## Abstract

Despite recent advances in extrusion bioprinting of cell-laden hydrogels, using naturally derived bioinks to biofabricate complex elastic tissues with both satisfying biological functionalities and superior mechanical properties is hitherto an unmet challenge. Here, we address this challenge with precisely designed biological tough hydrogel bioinks featuring a double-network structure. The tough hydrogels consisted of energy-dissipative dynamically crosslinked glycosaminoglycan hyaluronic acid (o-nitrobenzyl-grafted hyaluronic acid) and elastin through Schiff's base reaction, and free-radically polymerized gelatin methacryloyl. The incorporation of elastin further improved the elasticity, stretchability (~170% strain), and toughness (~45 kJ m<sup>-3</sup>) of the hydrogels due to the random coiling structure. We used this novel class of hydrogel bioinks to bioprint several complex elastic tissues with good shape retention. Furthermore, in vitro and in vivo experiments also demonstrated that the existence of elastin in the biocompatible bioinks facilitated improved cell behaviors and biological functions of bioprinted tissues, such as cell spreading and phenotype maintenance as well as tissue regeneration. The results confirmed the potential of the elastin-containing tough hydrogel bioinks for bioprinting of 3D complex elastic tissues with biological functionalities, which may find widespread applications in elastic tissue regeneration.

## KEYWORDS

biological functionalities, bioprinting, double-network, elastin, hydrogel, mechanical properties, toughness

## 1 | INTRODUCTION

Elastic tissues, including the heart, lung, auricle, trachea, and blood vessel, are abundant of fine elastic fibers.<sup>[1]</sup> Damages to such tissues by traumatic injuries or diseases have a significant impact on human health and life quality. For instance, microtia manifested mainly as partial or complete absence of elastic cartilage tissue of the external auricle. Compared to other congenital malformations, it has a relatively high incidence of 0.83–17.4 per 10,000 births worldwide.<sup>[2]</sup> To overcome the limitations and complications of autografts and allografts, tissue engineering emerged as a potential

alternative strategy, which evolved rapidly during the past decades.<sup>[3]</sup> Among all tissue engineering-oriented biofabrication approaches, three-dimensional (3D) bioprinting showed distinct advantages that allow the recreation of living constructs with complex structures by precisely positioning cells, biomaterials, and possibly biologic signaling molecules to mimic their anatomical characteristics and facilitate tissue regeneration.<sup>[4]</sup> Development of cell-laden 3D matrices, often termed bioinks, achieved rapid advancements in the past years.<sup>[5]</sup> Hydrogels are uniquely suited for acting as bioinks with the incorporation of cells in that they possess broadly tunable physical and chemical properties, provide structural support during fabrication, and can be customized to recreate the native extracellular matrix for relevant

Di Wang and Jinshi Zeng contributed equally to this study.

This is an open access article under the terms of the [Creative Commons Attribution](https://creativecommons.org/licenses/by/4.0/) License, which permits use, distribution and reproduction in any medium, provided the original work is properly cited.

© 2024 The Authors. *Aggregate* published by SCUT, AIEI, and John Wiley & Sons Australia, Ltd.

applications.<sup>[6]</sup> Biological polymers play crucial roles in cell-based bioprinting due to their intrinsic biocompatibility and minimal inflammatory responses *in vivo*.<sup>[6a]</sup> However, the use of single-component natural hydrogels have been limited by their insufficient mechanical performances, low printability, and poor biomimicry.<sup>[7]</sup> Most cell-laden natural hydrogels are brittle, having fracture energy on the order of  $10 \text{ J m}^{-2}$ ; hence, it is a major challenge to use them to bioprint load-bearing structures.<sup>[8]</sup> For instance, extracellular matrix-, gelatin-, or alginate-based hydrogel systems were applied in bioprinting 3D tissues with superior biofunctionalities at the expense of satisfied mechanical properties.<sup>[5a,9]</sup> As a result of the lack of suitable biological materials to formulate the bioinks, 3D bioprinting using natural hydrogels has faced difficulty building constructs that reproduce both the structural complexity and biological functionality of native tissues.<sup>[6a]</sup> To this end, the development of natural hydrogel systems with satisfying toughness for 3D bioprinting of certain desired tissues remains to be investigated.

The biological tough hydrogel designs offer an option for bioprinting cartilage, skin, and cardiovascular tissues for relevant tissue repair and regeneration given their enhanced mechanical properties compared to conventional hydrogels. Such designs require the introduction of dissipation mechanisms into the polymer networks, which allow the hydrogels to absorb the applied energy, deform without fracturing, and maintain elasticity during deformation.<sup>[10]</sup> Among all, the double-network (DN) design is one of the most popular strategies in forming tough hydrogels. After the DN hydrogel concept was initially introduced, tremendous research efforts have been made to take advantage of this concept to toughen the hydrogel systems.<sup>[11]</sup> Hydrogels created from DN polymers are interpenetrating networks that consist of two different polymers synthesized and intertwined together, carrying significantly higher toughness values than traditional hydrogels.<sup>[12]</sup> With increasing strain, a molecule chain network breaks at the isolated spot, while another chain network transmits stress effectively to toughen the hydrogel.<sup>[13]</sup>

However, increasing toughness of cell-laden hydrogels without compromising the cellular behaviors is challenging.<sup>[10,14]</sup> Recently, biological tough hydrogel systems based on DN design were developed to fill gaps in realizing both mechanical and functional regeneration simultaneously.<sup>[15]</sup> Nonetheless, few study concerns elasticity rehabilitation. In addition to providing the robust structural support, rehabilitating elasticity of bioprinted constructs to realizing biomimetic mechanical properties are of great importance as well, especially for complex elastic tissue regeneration. In mammals, elastin is the unique protein that serves this function.<sup>[1]</sup> Elastic fibers in elastic tissues can bear billions of cycles of extension and recoiling without mechanical failure, and therefore contribute to the elasticity and characteristic resilience of elastic tissues.<sup>[16]</sup> The random-chain model of elastin suggests that it behaves like a classical rubber, in which the polymer chains are kinetically free.<sup>[17]</sup> For this point, elastin-containing biomacromolecules have been applied to enhance the biomechanical properties of biomaterials.<sup>[17b,18]</sup> Besides, as an important regulator of cell behavior, elastin was reported as a potent mitogenic factor and facilitates the cells' proliferation and migratory.<sup>[19]</sup> Elastin-rich matrices were proved to be strongly chemotactic that provide cell binding motifs and support cell recruit-

ment and migration.<sup>[20]</sup> For instance, recombinant elastin was incorporated in the fabrication of scaffolds of engineered vascular conduits and cardiac and dermal tissues. In this way, elastin scaffolds successfully helped to recreate the elastic properties and biological functions of native arteries, myocardium, and skins.<sup>[21]</sup> However, naturally derived elastin was rarely reported used in biofabrication.

Herein, we present a stretchable elastin-containing double-network (eDN) tough hydrogel bioink system for extrusion bioprinting of engineered tissues with superior elasticity, stretchability ( $\sim 170\%$  strain), and toughness ( $\sim 45 \text{ kJ m}^{-3}$ ) compared to typical cell-laden hydrogels. The naturally derived bioactive prepolymer, composed of elastin, o-nitrobenzyl (NB)-grafted hyaluronic acid (HA-NB), and gelatin methacryloyl (GelMA), was crosslinked under ultraviolet (UV) light through phototriggered Schiff's base reaction and free-radical polymerization, respectively (Figure 1A). The strategy in this design to toughen the hydrogels was to utilize the well-established dissipation-induced toughening theory, which relies on associations between polymer chains to dissipate energy during deformation.<sup>[22]</sup> The system also exhibited good printability where the printed constructs had high resolution and biocompatibility with encapsulated cells. Finally, this bioactive hydrogel facilitated cellular activities, such as cell spreading and phenotype maintenance, as well as tissue regeneration.

## 2 | RESULTS AND DISCUSSION

### 2.1 | Design and physical characterization of biological eDN tough hydrogels

To regenerate engineered tissues with good mechanical performances and biological functionalities, we developed a cytocompatible bioink suitable for extrusion bioprinting. The natural polymer-based hydrogel significantly improved the toughness based on the dynamic sacrificial bonds in the DN. As reported, tough DN hydrogels are only obtained when the first network is tightly crosslinked, and the second network is sparsely crosslinked.<sup>[23]</sup> Here, in our hydrogel system, named GHE (G: GelMA, H: HA-NB, E: elastin), GelMA was relatively tightly crosslinked through free-radical polymerization to form the first network, while the sparse second network was generated between elastin and HA-NB through the dynamic Schiff's base reaction both triggered by UV light. GelMA was chosen for its biocompatibility, temperature-sensitive properties, tunable rheological properties, and printability.<sup>[24]</sup> Converted by o-nitrobenzene upon UV light illumination, the phototriggered-imine-crosslinking reaction in which o-nitrosobenzaldehyde groups quickly crosslink with amino groups distributed in elastin biomolecules occurs.<sup>[25]</sup> Additionally, after rapid photocrosslinking internally, GelMA had some additional amino groups available to further react with aldehyde groups of HA-NB. In this way, dual-crosslinking between the first and second networks was eventually formed to enhance the hydrogel mechanical performances.<sup>[26]</sup>

Hydrogel composed of GelMA and HA-NB (GH) and GelMA alone (G) were used as control groups in the study. As shown in Figure S1, all groups rapidly gelled in less than 5 s when exposed to UV ( $405 \text{ nm}$ ,  $30 \text{ mW cm}^{-2}$ ). In

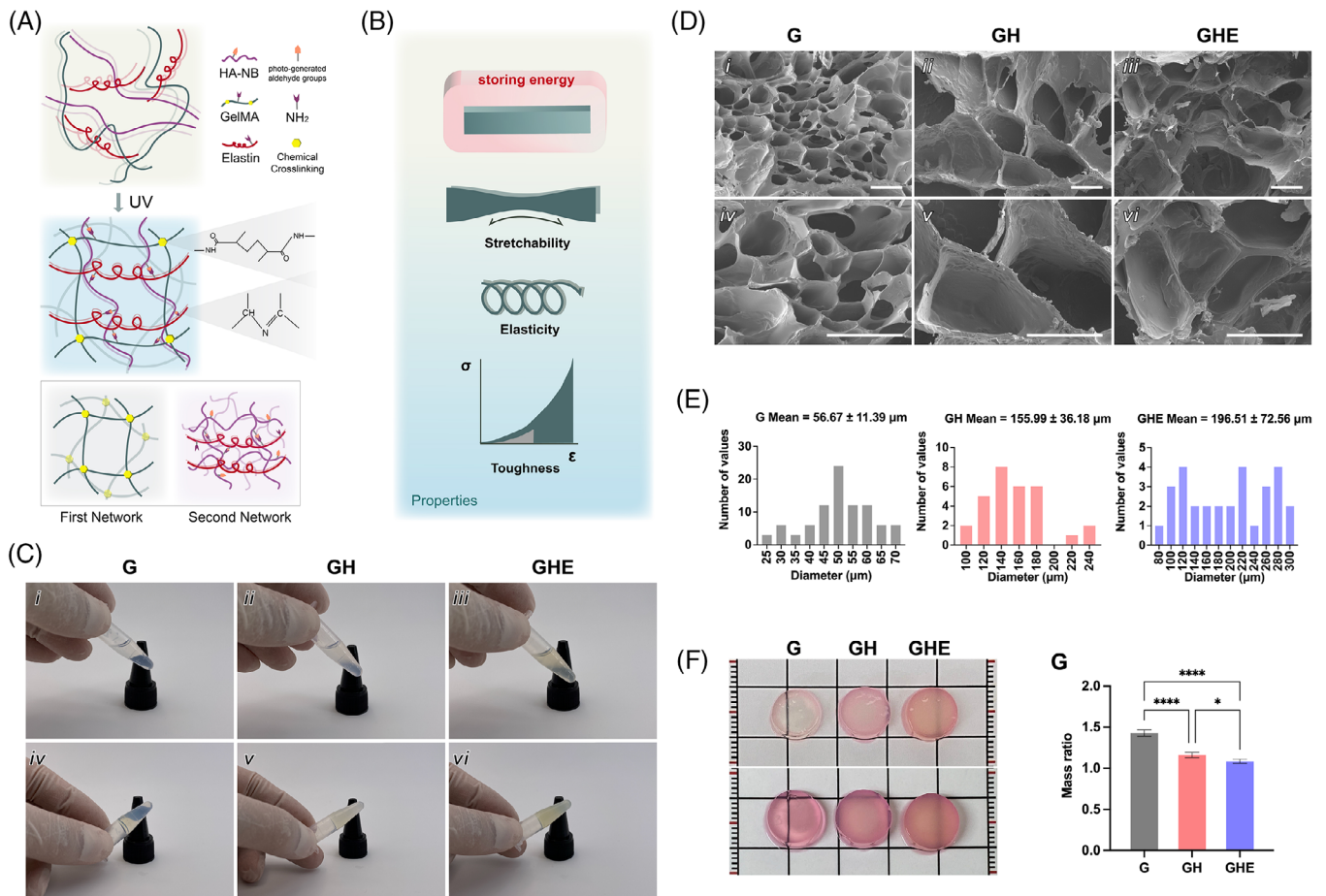


**FIGURE 1** Design and physical properties of hydrogels. (A) Schematics showing the elastin-containing double-network (eDN) hydrogels containing permanently crosslinked gelatin methacryloyl (GelMA) through free-radical polymerization as the first network as well as reversibly crosslinked elastin and glycosaminoglycan hyaluronic acid (HA-NB) through Schiff's base reaction. (B) Schematics showing the superior properties of the eDN hydrogels. (C) Visual inspection of different bioinks before and after crosslinking (G [GelMA alone], GH [G: GelMA, H: HA-NB], and GHE [G: GelMA, H: HA-NB, E: elastin]). (D) Scanning electron microscopy (SEM) images of different crosslinked hydrogels. Scale bars, 100  $\mu\text{m}$ . (E) Pore size distributions of different crosslinked hydrogels. (F) Physical appearances of different crosslinked hydrogels at 24 h after swelling. Scale bars, 1 cm. (G) Average mass ratios of different crosslinked hydrogels at 24 h after swelling. \* $p < 0.1$  and \*\*\*\* $p < 0.0001$  ( $n = 3$ ).

the sol phase, all precursors are presented as transparent liquid (Figure 1C, i–iii). After crosslinking, the G group kept its high transparency, which may be attributed to the lack of obvious light-scattering domains (Figure 1C, iv). GelMA hydrogels without these domains lack energy-dissipation mechanisms, making them soft and brittle. With the addition of HA-NB and elastin, cured hydrogels became inhomogeneous and turned opaque (Figure 1C, v and vi). Phase separation was supposed to be formed, which may further enhance the mechanical properties of hydrogels. However, this hypothesis needs to be proven in the future research.

Figure 1D (i–vi) shows scanning electron microscopy images of different hydrogels. The average pore size of pure GelMA hydrogel was  $56.67 \pm 11.39 \mu\text{m}$ , which was smaller than that of hybrid hydrogels ( $155.99 \pm 36.18 \mu\text{m}$  in GH and  $196.51 \pm 72.56 \mu\text{m}$  in GHE) (Figure S2). The pore size distributions of hydrogels are demonstrated in Figure 1E. In hybrid hydrogels, the existence of crosslinking from Schiff's bases reaction and additional polymers could likely decrease the crosslinking degree of GelMA due to high network hindrance, which increases, likely, the pore size of crosslinked hydrogels.<sup>[27]</sup> Hydrogel microstructure, especially pore size,

is an important factor for cell attachment and growth.<sup>[28]</sup> As reported, increasing the interconnective pore size of matrices, especially within the range of 80–120  $\mu\text{m}$ , contributing to better growth of chondrocytes and extracellular matrix (ECM) synthesis, resulting from diffusion of cells, nutrients, and waste products throughout macroporous scaffolds.<sup>[29]</sup> With a disperse pore size distribution of 80–300  $\mu\text{m}$ , GHE hydrogels are able to benefit cell behaviors due to enlarged space than pure GelMA. Additionally, culturing in Dulbecco's modified eagle medium (DMEM) for 24 h, hybrid hydrogels better maintained their morphologies as a swelling ratio of 1.16 (GH) and 1.08 (GHE) (Figure 1F,G), while that of pure GelMA was 1.43. Swelling ratios are also essential parameters of bioinks since they affect fidelity, resolution, and the cellular environment of bioprinted constructs.<sup>[30]</sup> With a relatively lower swelling ratio, constructs made of hybrid bioinks enjoyed less deformation after being cultured under liquid conditions for several days after bioprinting. The in vitro degradation profile of different hydrogels is demonstrated in Figure S3. Compared with G and GH hydrogels, GHE hydrogels were more resistant to degradation, which could be attributed to the increased crosslinks.

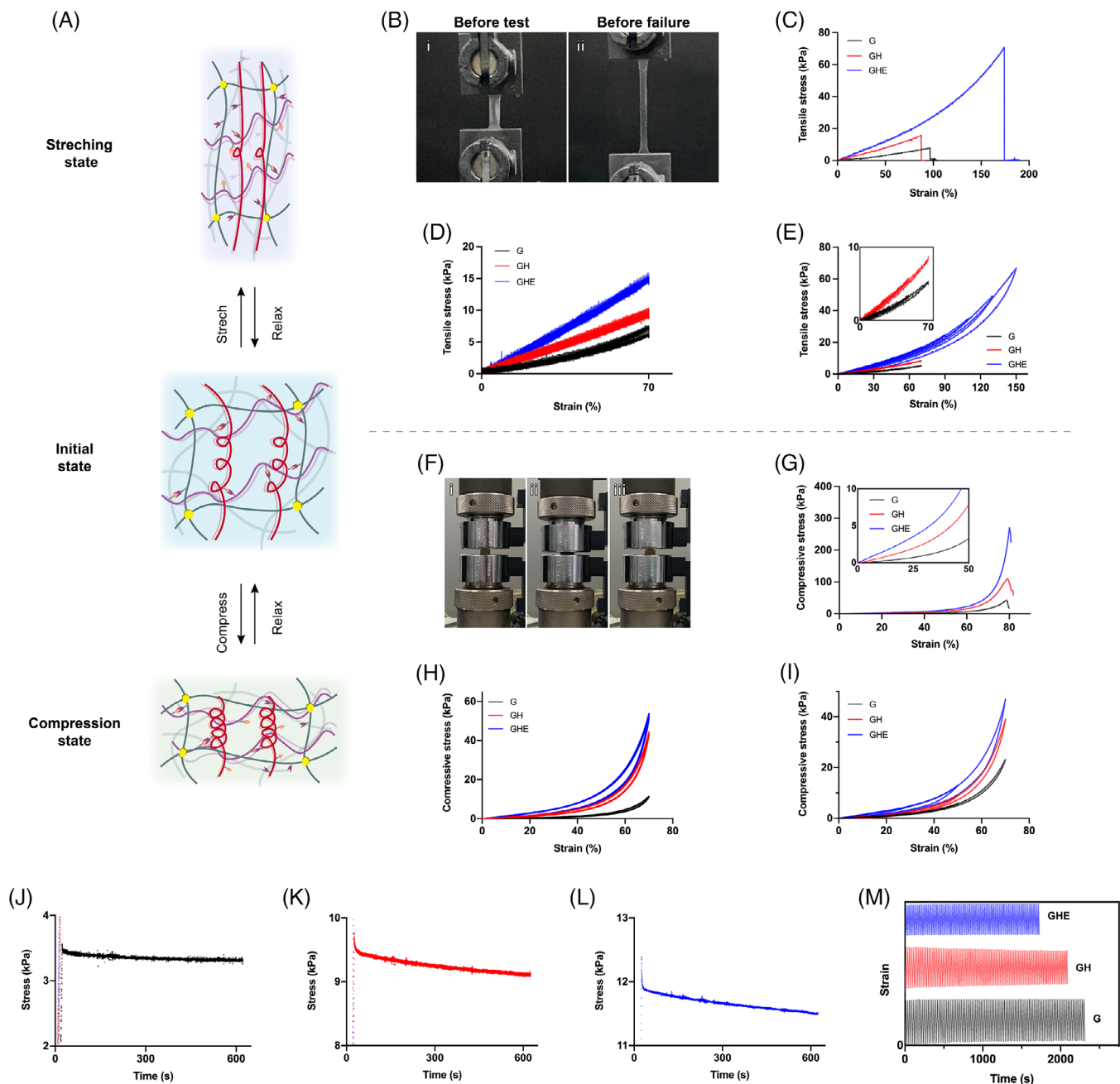


**FIGURE 2** Mechanical properties of hydrogels. (A) Schematics showing how the molecular chains of elastin-containing double-network (eDN) hydrogels respond to tensile and compressive stress. (B) Photographs of tensile tests for the eDN tough hydrogel films. (C) Tensile stress–strain curves of different hydrogel films. (D) Cyclic tensile tests of different hydrogel films (10 cycles with an applied strain of 70%). (E) Successive loading–unloading stress–strain curves of different hydrogel films with different maximum applied strains (from 10% to 150% for GHE [G: GelMA, H: HA-NB, E: elastin] and from 10% to 70% for GH [G: GelMA, H: HA-NB] and G [GelMA alone]). (F) Photographs of compressive tests for eDN tough hydrogel discs. (G) Compressive stress–strain curves of different hydrogel discs. (H) Cyclic compressive tests of different hydrogel discs (10 cycles with an applied strain of 70%). (I) Successive loading–unloading stress–strain curves of different hydrogel films with different maximum applied strains (from 10% to 70% for all groups). (J–L) Stress relaxation curves of different hydrogel discs. (M) Anti-fatigue curves of different hydrogel discs. GelMA, gelatin methacryloyl; HA-NB, o-nitrobenzyl-grafted hyaluronic acid.

## 2.2 | Mechanical properties of eDN tough hydrogels

The mechanical properties of the hydrogels were studied by tensile and compressive tests. As shown in Figure 2A,B, the GHE hydrogel sheets were stretched to large magnitudes under uniaxial tensile strains. They achieved an average failure strain of 167.93%, which was considerably more than that of G (89.29%) and GH (103.79%) (Figure S4). There were also notable differences among the three groups on both

tensile modulus and strength, leading to a high toughness of  $45.39 \text{ kJ m}^{-3}$  for the GHE DN hydrogel (Figures 2C and S4). The GH hydrogel was reported to be considered a type of DN hydrogel as well, as amino groups of GelMA would react directly with aldehyde groups of HA-NB.<sup>[25a]</sup> The DN design undoubtedly improved the mechanical performance of the GH hydrogel than that of the pure GelMA hydrogel.<sup>[15]</sup> However, in comparison, the GHE hydrogel had further profoundly enhanced its toughness, stiffness, ultimate strength, and extensibility. This is mainly due to the reversibility of its

independent second network, formed by the reaction between elastin and HA-NB, which positively contributed to energy dissipation in the hydrogel.

Additionally, the elastin protein also played a crucial role in reinforcing the hydrogel system. In this hydrogel system, the random coiling of elastin based on weak hydrophobic interactions made the molecular chains of the GHE hydrogel much more stretchable than that of G and GH groups.<sup>[31]</sup> With the coiling chains, elastin can be classified as a semiflexible biopolymer that assemble into filaments to produce fibrous hydrogels with a strain-stiffening response (Figure 2C).<sup>[32]</sup> It exhibits a nearly linear regime for moderate extensions and a sharp stiffening effect at large strain, where the acute realignment of fibers happens.<sup>[33]</sup> Moreover, the long and entangled chains of the animal-derived elastin may also contribute to the improved stiffness and toughness as the “mobile” chain entanglements allow mechanical energy to be dissipated in many chains and over long lengths.<sup>[34]</sup>

To further characterize the elasticity and energy-dissipation ability of the hydrogels, we performed cyclic tensile tests. We first stretched the hydrogel sheets to a strain of 70% at a strain rate of 50% min<sup>-1</sup> for 10 cycles to clearly show their resilience. The 70% strain was chosen to stay within the stretch limit of the weakest group (G), as determined from the uniaxial tensile tests. Figure 2D shows the loading–unloading stress–strain curves of the three different hydrogels. Cyclic tests suggested that both GHE and GH hydrogels had negligible hysteresis (Figure S5), which means that in the first 70% of tensile deformation, they could recover to their original shapes. Due to lack of reversible bonds and highly coiled structure, the G group presented a slightly visible (but not obvious) hysteresis when it was stretched to 70% strain and the chains began to rupture (Figure S5). This phenomenon might also result from the not highly crosslinked GelMA network (with a concentration of 5%, w/v) that the chains were not fully stretched to break enough bonds. We then conducted successive loading–unloading tests using increasing applied maximum strains of 10%–70% for G and GH, and 10%–150% for GHE (Figures 2E and S6). The results revealed that the GHE hydrogels began to have an obvious hysteresis loop at a strain of 110% (Figure S6). To investigate how the DN tough hydrogels would behave in large strains, we subsequently stretched the GHE hydrogels to a strain of 150% for 10 cycles (Figure S7). A higher hysteresis was observed in the first cycle as knotted and entangled polymer chains unraveled and crosslinked GelMA chains ruptured, causing permanent damage. The hydrogel’s stress softening during the first few cycles was suggestive of permanent structural changes that tapered off with repeated deformation. However, no obvious hysteresis loop could be found beyond the first cycle, which was likely due to the restructuring of chains resulting from repeated coiling and uncoiling of elastin protein and dynamic covalent crosslinking of the second network.<sup>[35]</sup> Before stretching, elastin existed in a high entropic state and an unfolding of the chain would decrease the polymer’s entropy.<sup>[17a,32]</sup> Stretching orientated the chains and limited the overall entropy of the system, which saved the restoring force for recoiling.<sup>[36]</sup> Moreover, during stretching, the elastin chains were deformed to expose the hydrophobic side domains, increasing system energy, which was then released through recoiling.<sup>[37]</sup> These results manifested that although

the first network (GelMA) could be damaged during deformation, the stretchy second network would maintain the material integrity.

Compression tests also indicated the same tendency in certain quantitative characterizations (Figures 2A,F,G and S8). The GHE hydrogel bulks returned to the initial status after the relief of a high compressive strain of 70% (Figure 2F). Among the three groups, the GHE hydrogels had the highest compressive modulus (19.85 kPa), strength (204.78 kPa), and toughness (24.58 kJ m<sup>-3</sup>). The GHE hydrogel discs not only had significantly improved stiffness, they also could bear ~80% compressive deformation without rupture. To investigate the hydrogels’ resilience under compression conditions, we conducted cyclic compressive tests on them (Figure 2H). We compressed the hydrogel discs to a strain of 70% at a strain rate of 50% min<sup>-1</sup> for 10 cycles. Notably, the results seemed different from tests under tensile conditions. Compared to the other two types of hydrogels, the GHE hydrogels had obvious hysteresis loops throughout the 10 cycles. However, they did not show visible signs of plastic deformation. Instead, the compressed GHE discs entirely returned to the resting length and back to their original shape instantly (Figure 2H). Re-compression stress curve almost matched the previous extending curve, reflecting no (or very few) loss of stiffness. As such, the GHE hydrogels owned the largest hysteresis loop and highest ultimate stress, demonstrating that much energy had been stored in hydrogels during loading–unloading. With the 10 cycles of loading–unloading, the ultimate stress only had a slightly decreasing trend. While in the G and GH groups, after the first compression cycle, the hydrogels became weaker (stress softening) if the following tests were applied immediately. As shown in Figure 2I, successive loading–unloading compression tests using increasing applied maximum strains of 10%–70% for all groups were conducted. Each loading curve of GHE exactly matched and covered the previous loading curve and went back to the original points. We hypothesized that in the limited compression strain, the coiling of elastin had no space to deform, while dynamic covalent bonds dominated energy dissipation in our DN hydrogels. After the removal of stress, the elastic network of the GHE hydrogels helped to drive fast recovery.

To study the viscoelasticity of the hydrogels, we in addition conducted stress relaxation experiments with a constant compressive strain of 50%. Besides energy dissipation, stress relaxation is a main feature that indicates the viscoelastic response of the material.<sup>[38]</sup> Fast viscoelastic stress relaxation pronouncedly promotes many biological behaviors of cells encapsulated in hydrogels, including cell proliferation, spreading, and differentiation.<sup>[27,39]</sup> As demonstrated in Figures 2J–L and S9, the GHE discs had the highest relaxation modulus of 96.36 kPa, exceeding those of GH at 56.96 kPa and G at 26.7 kPa. Benefitting from the DN hydrogel design and the incorporation of elastin, the GHE hydrogels enjoy a striking increase in the rate of stress relaxation.

We next explored the anti-fatigue performance of the hydrogels by a creep model using constant loading stress of 20 kPa for 100 uninterrupted cycles. The loading stress was determined by the weakest hydrogel and kept constant among all groups. As shown in Figure 2M, the GHE discs could easily recover to their original shapes even after repeating 100

cycles of mechanical loading. However, irreversible shape changes were observed in both other two hydrogel types in that the compressive stress decreased by applied cycle number counted. The observations suggested that the GHE DN hydrogels owned favorable anti-fatigue properties.

The mechanical performance characterizations demonstrated that the biological GHE DN tough hydrogels had significantly improved stiffness, stretchability, toughness, elasticity, anti-fatigue property, and viscoelasticity, and could be used for elastic tissue regeneration.

### 2.3 | Bioprinting of 3D elastic complex constructs using eDN tough hydrogels

To test the printability and set printing parameters, the rheological properties of three precursors as bioinks were measured. All hydrogels were found to exhibit temperature-dependent viscoelastic properties due to the thermoresponsive GelMA component (Figure 3A). An increase of temperature from 4°C to 40°C resulted in a gradual decrease of the  $G'$  and crossover with  $G''$  at a critical gelation temperature, indicating a gel–sol transition.<sup>[40]</sup> Among all, the GHE precursor had the highest transition temperature of approximately 24°C. The complex viscosity of the GHE precursor decreased two orders of magnitude beginning at around 18°C. At low temperatures, such as 10°C, the viscosity dramatically increased and much higher pressure was needed to extrude the bioink, which could harm the viability of encapsulated cells. For the bioink to be successful at printing, it must possess sufficient viscosity, and shear-thinning property which allows smooth flow of the bioink during extrusion. Here in the study, shear-thinning behavior was observed rheologically using steady shear flow sweeps from low to high shear rates (Figure 3B). At the shear rate of 0.1 s<sup>-1</sup>, GHE had a high apparent viscosity (47,770.1 mPa s), which was about five times higher than that of GH (9686.7 mPa s) and over 400 times higher than that of G (111.8 mPa s). In all groups tested, the viscosity decreased approximately two orders of magnitude with increasing shear rates. The result indicates that the hydrogel can flow under high shear rates present in the print nozzle, but then undergo time-dependent recovery of their initial properties. The shear-thinning and cell-benign thermoresponsive properties ensured that the GHE bioinks could be used for extrusion bioprinting.

After several attempts of printing, we fixed most of the printing parameters. An inner diameter of 23 G blunt needle was chosen as the extrusion nozzle. Based on rheology test results, the temperature of the bioink carrier was reduced and maintained at 20°C, and the temperature of the receiving platform was set as 18°C. Extrusion pressure (0.6–1 bar) and print head moving speed (13–15 mm s<sup>-1</sup>) were adjusted according to the condition of extruded microfibers. Then, we compared the printability of bioinks of G and GHE by evaluations of extruded filament status on the nozzle tip and integrity of the first two layers of the printed construct (Figure 3C). When the bioink of pure 5% (w/v) GelMA was printed under 20°C and 0.7 bar of pressure, it would demonstrate the droplet morphology at the nozzle tip. Extruded filaments of both first and second layers fused to form a square (Figure 3C, i–iii). This was consistent with reported

results that GelMA precursors with insufficient viscosities formed blobs at the needle tip resulting in the final structure sagging on the substrate.<sup>[41]</sup> Equipping the bioink of 5% GelMA and a 23 G needle with an inner diameter of 0.34 mm, the bioprinter extruded a filament of 2.3 mm under 0.6 bar of pressure under a nozzle moving speed of 14 mm s<sup>-1</sup>. The pressure gradually increased from 0.7 to 1.0 bar, and the diameter of the filaments increased from 2.7 to 5.7 mm accordingly, which was far from the desired resolution (Figure 3C, iv). We then tried to use lower temperatures and good results were achieved only when the bioink of GelMA was cooled down below 8°C. However, extruded fibers in a square construct fused on some intersecting sites or collapsed on uncross sites, making it unfeasible to manufacture an integral 3D construct (Figure S10). When it turned to bioink of GHE, smooth and uniform filaments were continuously extruded, resulting in a standard grid construct with clearly distinguishable layers (Figure 3C, v–vii). Figure 3C (viii) shows diameters variation (0.4–1.2 mm) with changes of pressure (0.6–1.0 bar) under the same movement speed and size of a nozzle (23 G).

In addition to viscosity, bioink should possess adequate viscoelasticity to support layer deposition, especially for complex constructs. It is a bottleneck for most soft hydrogels that bioinks with insufficient storage moduli would collapse after printing as they are unable to hold their own weights.<sup>[8]</sup> Benefiting from the excellent mechanical properties of GHE hydrogels, all bioprinted constructs exhibited superior appearances. Using the GHE bioinks, we attempted to print three different complex organ analogs and quantified the maintenance of 3D morphologies of the printed constructs by 3D deviation comparisons. As the human nose looks like a conical structure, it was the arguably simplest object to be printed in that almost no overhanging part needed to be considered during printing. Figure 3D presents the different views of a printed 34-layer nose and different layers of the construct. Extruded microfibers were neatly arranged layer by layer and an integral construct was smoothly printed without collapse or deficiency. A deviation chromatogram displayed the morphological similarity, with a 93.87% deviation within 2 mm (Figure 3F), indicating that nose morphology was largely reconstructed. Compared to printing “small-on-large” layers of the nose, the existence of cranioauricular angle makes printing detailed units of a human ear to be a harder task.<sup>[42]</sup> In layer-on-layer printing approaches, support structures are usually needed to help temporarily provide mechanical support and hold the print up during the printing process overhanging constructs.<sup>[43]</sup> As shown in Figure 3G, 23 layers of a human auricle with a cranioauricular angle of 120° were printed. No support structure was built. Extruded microfibers were exposed to UV light for ~3 s in each layer, and crosslinked hydrogels held their position till post-radiation of UV light after printing was finished. The deviation of printed auricle within ±2 mm reached 94.75% (Figure 3H,I). Made up of thyroid cartilage, cricoid cartilage, and tracheal cartilage, the shape of the human trachea is not a regular tubular structure.<sup>[44]</sup> We then tried to print an integrated cricoid and tracheal cartilage construct with 40 layers using GHE bioinks (Figure 3J). Although similar problems were faced as we printed human ear, satisfying constructs were finally achieved with a ±2 mm deviation of 96.50% (Figure 3K,L).

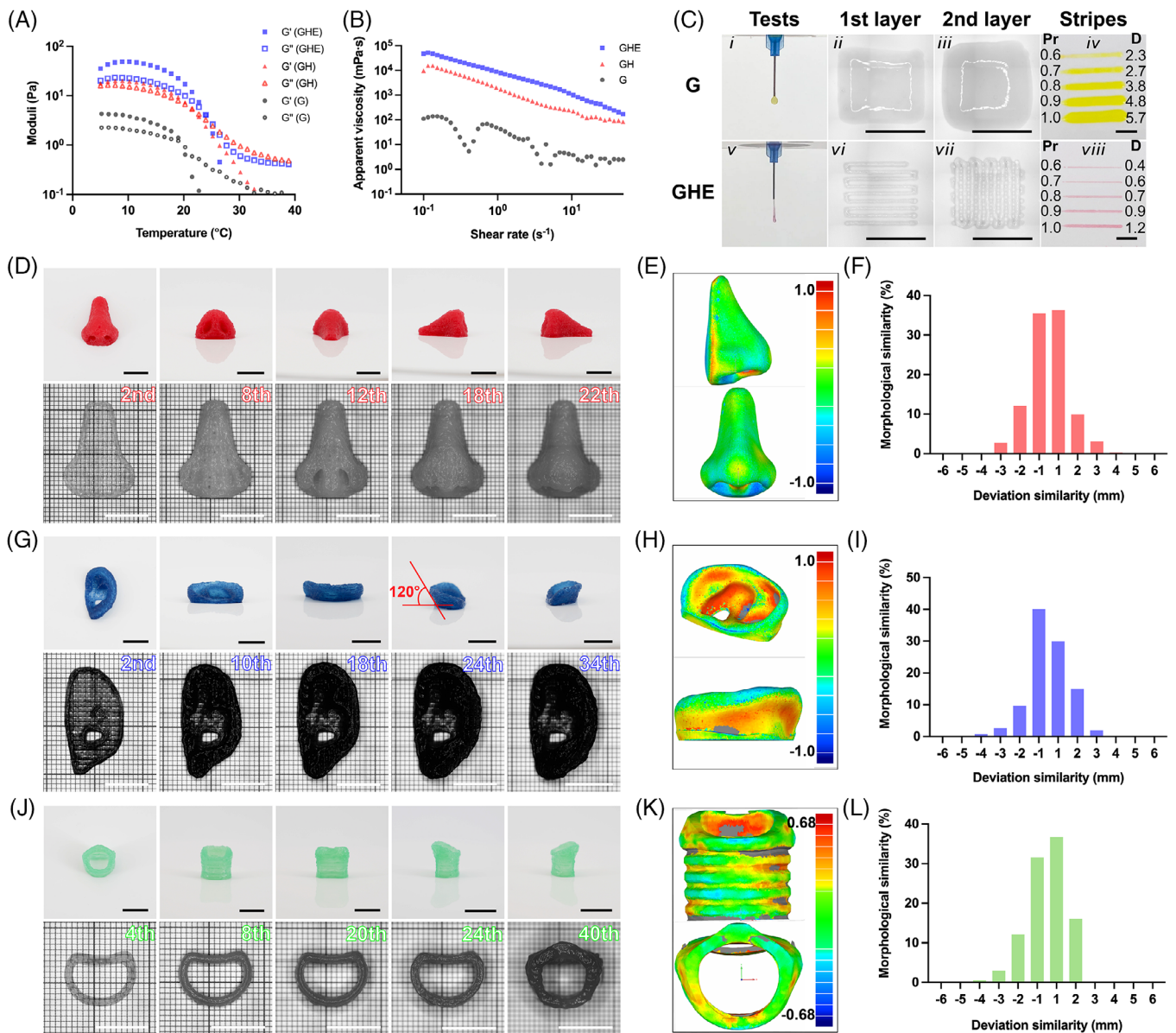


**FIGURE 3** Printability of elastin-containing double-network (eDN) hydrogel bioinks. (A) Storage moduli (solid marks) and loss moduli (open marks) as a function of temperature for different hydrogel bioinks. (B) Apparent viscosities as a function of shear rate for different hydrogels at 37°C. (C) Photographs of extruded filaments and printed mesh constructs using different bioinks. Scale bars, 1 cm. (D) Photographs of general views and different layer views of printed human nose constructs using eDN bioinks. Scale bars, 1 cm. (E) Three-dimensional reconstruction of the printed human nose. (F) Morphological deviation comparison of the printed human nose. (G) Photographs of general views and different layer views of printed human auricle constructs using eDN bioinks. Scale bars, 1 cm. (H) Three-dimensional reconstruction of the printed human auricle. (I) Morphological deviation comparison of the printed human auricle. (J) Photographs of general views and different layer views of printed human tracheal constructs using eDN bioinks. Scale bars, 1 cm. (K) Three-dimensional reconstruction of the printed human tracheal. (L) Morphological deviation comparison of the printed human tracheal.

## 2.4 | Biological characterizations of chondrocytes embedded in eDN tough hydrogels

Concerning the structural complexity and the outstanding toughness, we bioprinted and regenerated the auricular cartilage in the following sections as a demonstration. Elastic cartilage, which contains elastic fiber networks, mainly presents in the auricle, larynx, and eustachian tube. Typically, the tissue does not bear high mechanical loads but provides support with moderate elasticity and flexibility.<sup>[45]</sup> Due to the lack of blood supply, elastic cartilage has a very limited capacity to regenerate or be repaired compared to other connective tissues.<sup>[46]</sup>

To characterize the biological functionalities and tissue regeneration abilities of the bioprinted constructs by elastin-containing DN tough hydrogels, auricular chondrocytes were harvested from Bama miniature pigs. To direct bioprint cell-laden constructs for cell staining characterizations, bioinks stock solution was mixed with  $5 \times 10^6 \text{ mL}^{-1}$  of chondrocyte suspension, followed by loading into a 20°C carrier and extruded as droplets to form a bulk hydrogel (Figure 4A). The cell-benign hydrogel protected cells during bioprinting, reducing shear stresses and subsequent cell membrane damage, increasing cell viability in the bioprinted constructs.<sup>[6a]</sup> Bulk hydrogels were first used to test bioinks' cytocompatibility. Live/dead staining indicated that no significant difference can be observed among three types of

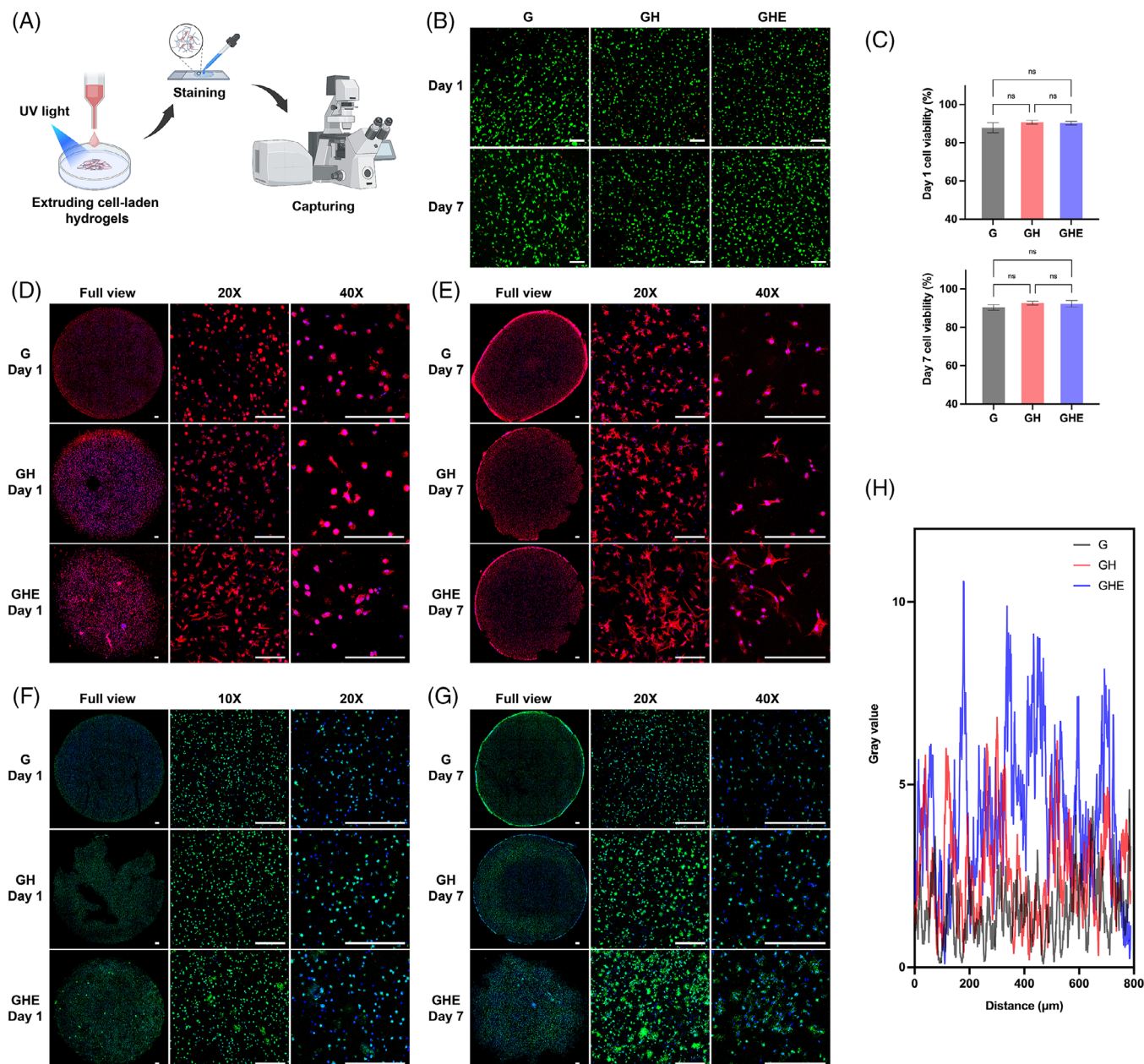


**FIGURE 4** Biological characterizations of chondrocytes encapsulated in different hydrogels. (A) Schematics showing the process of staining cells embedded in printed hydrogel discs. (B) Fluorescence microscopic images of live/dead staining for chondrocytes encapsulated in different hydrogels at indicated time points. (C) Quantified viability of chondrocytes at indicated time points. Scale bars, 200  $\mu\text{m}$ . ns, no significant difference. (D) Fluorescence microscopic images of F-actin staining for chondrocytes encapsulated in different hydrogels on day 1. Scale bars, 200  $\mu\text{m}$ . (E) Fluorescence microscopic images of F-actin staining for chondrocytes encapsulated in different hydrogels on day 7. Scale bars, 200  $\mu\text{m}$ . (F) Fluorescence microscopic images of collagen type II (COL II) staining for chondrocytes encapsulated in different hydrogels on day 1. Scale bars, 200  $\mu\text{m}$ . (G) Fluorescence microscopic images of COL II staining for chondrocytes encapsulated in different hydrogels on day 7. Scale bars, 200  $\mu\text{m}$ . (H) Fluorescence intensity curves of expressed COL II on day 7 in different hydrogels.

hydrogels in days 1 and 7 cell viabilities, which exceeded 85% and 89%, respectively (Figure 4B,C). Although extruding tough hydrogel required higher shear force, it did not damage cells encapsulated in the GHE bioinks during bioprinting, which is accordance with other reports.<sup>[47]</sup> Live/dead staining also manifested that the GHE bioinks had good cytocompatibility.

Chondrocyte volume and morphology profoundly influence the stability of the chondrocyte phenotype.<sup>[48]</sup> Cellular shape, cytoskeletal configuration, and regulation were confirmed to play important roles in the process of chondrogenesis.<sup>[49]</sup> Cellular proliferation, morphology, and cytoskeleton organization in the hydrogels were visual-

ized by performing immunofluorescence staining of F-actin. The results showed that most chondrocytes in the G and GH hydrogels maintained spherical morphologies without spreading during culture on day 1, however, cells in the GHE hydrogels started to spread out at the same time point (Figure 4D). On day 7, the chondrocytes in all hydrogels exhibited observable spreading (Figure 4E). Among them, the GHE hydrogel displayed the largest cell volume and tendency of cell aggregation. It is well established that cellular activities are exquisitely sensitive to the stiffness of the cell-encapsulating matrix as it has been proven to regulate cell spreading, migration, proliferation, gene expression, and differentiation.<sup>[50]</sup>

GelMA-based bioinks, with a respective concentration higher than 7% (w/v), have been limited to use due to the high Young's modulus and the high degree of crosslinking would inhibit cell spreading and migration and resulted in weak F-actin filament network formation.<sup>[51]</sup> Notably, although the GHE hydrogels had a much higher modulus than the 5% (w/v) GelMA, chondrocytes extensively spread in them. The enlarged pore size in GHE hydrogels might be one reason, which offered the cells more space to elongate and set them free from intense crosslinking as in other stiff hydrogels, such as 10% (w/v) GelMA, which has a similar modulus of ~20 kPa.<sup>[52]</sup> Beyond stiffness, it has been reported that viscoelastic properties can also have a profound effect on cellular behaviors and good spreading was observed in physiological extracellular matrices with quick stress relaxation.<sup>[27,53]</sup> Compared to the other groups, GHE exhibited the highest relaxation modulus (Figure S9). As a result, faster stress relaxation of the GHE bioinks might increase cell spreading and proliferation.

Chondrocyte phenotypic stability is essential as the chondrogenic type normally synthesizes a matrix principally comprised of collagen type II (COL II) and aggrecan.<sup>[48]</sup> After 1 week of *in vitro* chondrogenic culture, the majority of cells in the three groups showed COL II expression (Figure 4F,G). Immunofluorescence labeling of COL II appeared most intense in the GHE group compared to the other samples at the same cell seeding density and capture parameters of the microscope (Figures 4H). It was hypothesized that elastin protein in the bioprinted constructs interacts immediately with chondrocytes and provided an improved environment for cell attachment, proliferation, and differentiation and thus promoted ECM production. This phenomenon was reported in a published study,<sup>[54]</sup> in which the authors used hydrogels containing the  $\kappa$ -elastin with a low concentration for the bioengineering of elastic cartilage. They figured out that the chondrocytes suspended in hydrogels with  $\kappa$ -elastin produced more extracellular matrix than those embedded in hydrogels without  $\kappa$ -elastin. These results further revealed that biological elastin-containing DN tough hydrogels facilitate the maintenance of chondrocyte phenotypic stability and the process of chondrogenesis.

## 2.5 | *In vivo* elastic cartilage regeneration of cell-laden constructs

The regenerative potential of the GHE hydrogels laden with auricular chondrocytes was evaluated in nude mice. Cell-laden discs made from three types of hydrogels were casted using polydimethylsiloxane (PDMS) models. The hydrogel discs were implanted beneath the skin and explanted after 2 months to compare the formation of cartilage among the three groups. As a demonstration in Figure 5A, discs made of pure GelMA were too soft to withstand the skin tension that they aggregated and lost the original round shape immediately after implantation. In the next 2 months of *in vivo*, the GelMA discs degraded without chondrogenesis. Although the GH discs maintained their basic shape, they lost ~24% of the initial weight with unsatisfied cartilage-like tissue formation (Figures 5B and S11A). In contrast, no significant weight changes were observed in the GHE group (Figure S11B). Apparently, porcelain white tissue generated

in the GHE hydrogels, was considered as the formation of milky white cartilage-like tissue. Hematoxylin–eosin (H&E) and safranin O staining showed that cells in the GHE hydrogel formed classical chondrocyte lacunae structure with cartilage-specific ECM deposition, but the fewer can be observed in the GH group (Figure 5C).

Finally, as shown in Figure 5D, we bioprinted human ear-shaped constructs (~2 cm in length) with fine fidelity using cell-laden GHE hydrogels and transferred them into nude mice ( $n = 5$ ). Less satisfied ear-shaped constructs were also bioprinted using GH hydrogels as the control group ( $n = 3$ ). By 3 months of culturing *in vivo*, the gross appearance of most implanted GHE constructs flattened slightly. Their deformation might be attributed to insufficient stiffness (~20 kPa) and long-term pressure from skin tension. However, they still maintained integrity and the basic auricular shape, which was to credit of superior toughness of GHE hydrogels. The whole explanted constructs presented as milky white cartilage-like tissue. In contrast, the GH engineered ears turned to 2D constructs and completely missed their original shapes. A GH implant even broke during culturing due to insufficient toughness of GH hydrogels. By 3 months *in vivo*, the mass of the engineered ear using GHE hydrogels still did not change significantly, mainly due to the balance of new cartilage tissue regeneration and degradation of the naturally derived biomaterials (Figure 5E, i). While, the GH engineered ears lost ~55% initial weights in that most of the hydrogels degraded but the new cartilage tissue did not regenerate well (Figure 5E, ii). Histology staining revealed that preliminarily mature cartilage-like tissue was formed throughout GHE auricular constructs, and positive staining of elastic fibers by Victoria blue further confirmed their elastic cartilage characterization (Figure 5F). In contrast, GH auricular constructs failed to form elastic cartilage-like tissue (Figures S12–S14). Even osteogenic differentiation was observed in a GH auricular construct. Segregated areas of cells and hydrogels were observed on histology staining images. This phenomenon could be a result of the inhomogeneous mixing of cell suspensions and the bioinks of the slightly high viscosity. We then performed immunohistochemical staining of COL II and elastin to verify the formation of elastic cartilage-like tissue, and results showed high expression of both elastic cartilage-specific proteins (Figure 5G). As shown in Figure 5H, collagen content of bioprinted auricle-shaped constructs explanted at the end of third month reached ~80% of native cartilage, which apparently rose and was higher than that of cell-laden GHE discs cultured *in vivo* for 2 months. In comparison, the cell-laden GH discs showed obviously low-level expression of collagen when explanted after 2 months. Glycosaminoglycan (GAG) content also exhibited the same trend. Although GAG content of bioprinted auricle-shaped constructs did not reach the level of native cartilage, it doubled that 2 months GHE discs after cultured for 1 more month *in vivo*. The quantitative analysis revealed that, compared to GH hydrogels, GHE significantly facilitate secretion and deposition of ECM of chondrocytes.

## 3 | CONCLUSIONS

In summary, we developed DN tough hydrogel bioactive bioinks consisting of GelMA, HA-NB, and animal-derived

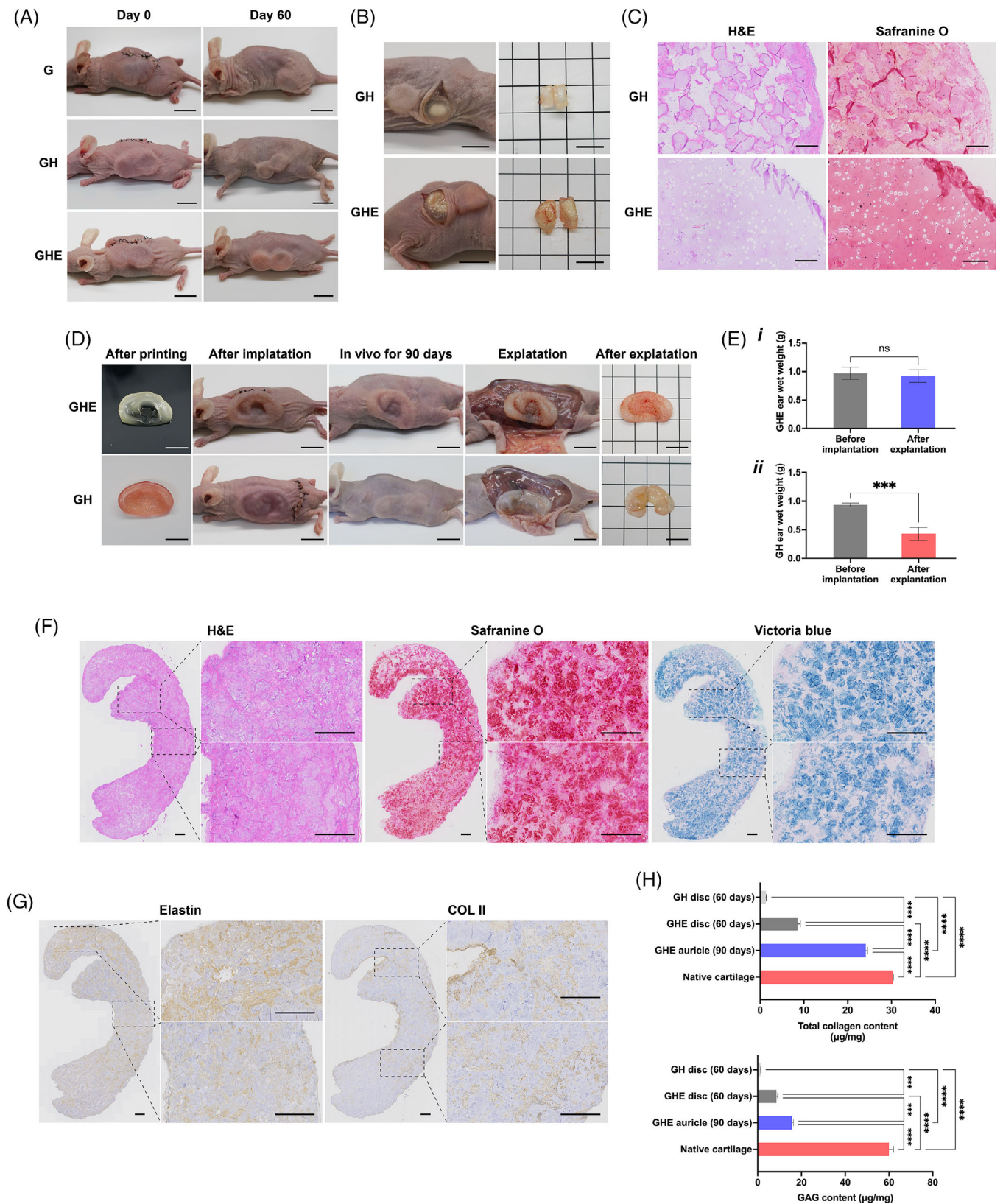


**FIGURE 5** In vivo elastic cartilage regeneration. (A) Gross view of cell-laden casted hydrogel discs implanted in nude mice for 60 days. Scale bars, 1 cm. (B) Gross view of explanted hydrogel discs. Scale bars, 1 cm. (C) Histology staining of explanted hydrogel discs. Scale bars, 100  $\mu$ m. (D) Implantation and explantation of bioprinted cell-laden GHE (G: GelMA, H: HA-NB, E: elastin) tissue engineered auricular cartilage. Scale bars, 1 cm. (E) Wet weight comparison of bioprinted auricular cartilage before implantation and after explantation. ns, no significant difference. (F) Histology staining of bioprinted GHE auricular cartilage. Scale bars, 1 mm. (G) Immunohistochemical staining of bioprinted GHE auricular cartilage. Scale bars, 1 mm. (H) Quantitative of total collagen and glycosaminoglycan (GAG) content of native cartilage and explanted engineered tissues. \*\*\* $p < 0.001$  and \*\*\*\* $p < 0.0001$  ( $n = 3$ ). COL II, collagen type II; GelMA, gelatin methacryloyl; HA-NB, o-nitrobenzyl-grafted hyaluronic acid; H&E, hematoxylin-eosin.

elastin with suitable rheological properties and cell-benign crosslinking for extrusion bioprinting of engineered complex elastic tissues. The GHE hydrogels exhibited superior and mechanical properties, including toughness, stretchability, elasticity, anti-fatigue ability, viscoelasticity, and high resilience in responding to deformation. Using GHE hydrogels as bioinks, we bioprinted complex elastic tissues with satisfied fidelity, and they maintained long-term integrity and general shape *in vivo*. Additionally, the bioactive bioinks were proven to facilitate cell behaviors and biological functions of bioprinted tissues. Specifically, they were beneficial to cell spreading and phenotype maintenance, and as an illustration, promoted elastic cartilage-specific ECM deposition and elastic cartilage-like tissue formation. However, our bioink is not without limitations. For example, despite enhanced high toughness and elasticity, the bioprinted construct cannot bear skin tension as expected due to their insufficient stiffness. Additional efforts are being devised to further improve the bioink formulations. Besides, we should use more cell types to verify some phenomenon. Our further studies are focusing on developing cell-benign high-stiffness bioinks without limiting cell spreading, migration, or proliferation.

## 4 | EXPERIMENTAL

### 4.1 | Materials and animals

The study did not generate new unique reagents. Live/dead viability/cytotoxicity kit, dialysis membrane (molecular weight cutoff: 12,000–14,000 Da), bovine serum albumin, Dulbecco's phosphate-buffered saline (DPBS), DMEM, penicillin–streptomycin–neomycin (PSN) antibiotic, trypsin–ethylenediaminetetraacetic acid, 4',6-diamidino-2-phenylindole (DAPI), and antibiotic–antimycotic solution stabilized were purchased from Thermo Fisher Scientific. Mouse anti-elastin antibody, rabbit anti-COL II antibody, goat polyclonal secondary antibody against mouse IgG-H&L (Alexa Fluor 488), and DAB detection IHC kit were purchased from Abcam. Safranin-O and Victoria blue staining kit were purchased from Beijing Solarbio Science & Technology Co., Ltd. TRITC-Phalloidin kit was purchased from Yongqinquin Intelligent Equipment Co., Ltd. Unless otherwise mentioned, all other materials were purchased from Sigma–Aldrich. Bama miniature pigs (female, 6 months old) and nude mice (male and female, 6 weeks old) were purchased from Beijing Vital River Laboratory Animal Technology Co., Ltd. Animal experiments were approved by the Animal Care and Experiment Committee of Plastic Surgery Hospital (Institute), Chinese Academy of Medical Sciences, and Peking Union Medical College.

### 4.2 | Synthesis of GelMA and HA-NB

GelMA was synthesized following the previously described protocol we introduced.<sup>[15]</sup> Briefly, 10.0 g of type-A gelatin from the porcine skin was added into 100 mL of DPBS and dissolved at 50°C under a magnetic stirrer for 30 min. Then, 5.0 mL of methacrylic anhydride was added dropwise to the gelatin solution and kept stirring at 50°C for 3 h. The reaction

was quenched by 100 mL of warm DPBS (40°C). Next, the reaction product was dialyzed against distilled water at 40°C for 5 days using a dialysis membrane. Last, the solution was filtered by a 0.2- $\mu$ m filter and lyophilized to yield a white porous foam, which was stored at –20°C for further use.

HA-NB was synthesized according to publications.<sup>[25a,25b]</sup> Briefly, HA was dissolved in 100 mL, 0.1 M 2-morpholinoethanesulfonic acid solution, and 0.4 g 4-(4,6-dimethoxy-1,3,5-triazin-2-yl)–4-methyl morpholinium chloride was added inside. An amount of 60 mg NB was dissolved in dimethyl sulfoxide, added into the above solution, and stirred for 24 h in the dark at room temperature. Then, the solution was dialyzed against deionized water for 4 days followed by lyophilization to yield a slightly yellow solid foam, which was stored at –20°C for further use.

### 4.3 | Extraction of elastin

Elastin was extracted from porcine aorta by oxalic acid extraction, according to a report.<sup>[55]</sup> Harvested porcine aorta was defatted, boiled, dried, and broken up. NaCl was added to remove impurities. Then, samples were dried at 60°C and broken up again. After digestion with oxalic acid in a steam bath at 100°C, the filtrate was cooled to room temperature, centrifuged, and filtered through a 0.2- $\mu$ m membrane. After dialyzing through a dialysis membrane, elastin was collected by lyophilization and stored at –20°C. The elastin digested by oxalic acid has the molecular weight distribution above 130 kDa; the viscosity of 1% (w/v) elastin was 4.8 mPa s.

### 4.4 | Hydrogel films and discs fabrication

The biopolymers were all dissolved in DPBS or culture medium at 37°C overnight to prepare the hydrogel precursors. Three different hydrogels were prepared as followings: G, 5% (w/v) GelMA; GH, 5% (w/v) GelMA and 1% (w/v) HA-NB; GHE, 5% (w/v) GelMA, 1% (w/v) HA-NB, and 1% (w/v) elastin. Liquid-form hydrogel precursors were sandwiched between two glasses by 0.4-mm plastic spacers, followed by curing under UV light for 1 min. The obtained hydrogel films were cut for further experiments. To cast hydrogel discs, precursors were poured in cylinder PDMS molds and cured under UV light for 1 min.

### 4.5 | Morphology characterization, swelling tests, and degradation analysis of hydrogels

The morphology of the fracture surface of the hydrogel constructs was observed using scanning electron microscope (Philips XL-30) at an accelerating voltage of 15 kV after lyophilization. The pore size and the porosity of the hydrogel constructs were analyzed by ImageJ software ( $n = 3$  per group).

The casted hydrogel discs (diameter = 8 mm and height = 3 mm) were recorded as the initial wet weight ( $W_0$ ). The hydrogels were fully immersed in culture medium for 24 h till swelling equilibrium ( $n = 4$ ), and the final wet weight was recorded as  $W_t$ . The swelling ratio was calculated

according to the following formula:

$$\text{Swelling ratio (\%)} = \frac{W_t}{W_0} \times 100\%$$

The casted hydrogel discs were further used in degradation analysis. Lyophilized hydrogel discs were weighed ( $W_0$ ) and incubated in phosphate-buffered saline (PBS). All samples were kept in the shaker incubator (120 rpm) for 1, 2, 3, 4, 5, and 6 weeks at 37°C. The liquid was replaced every week. At determined time points, hydrogel discs were picked out for lyophilization (24 h) and weighed ( $W_t$ ). The degradation rate was calculated according to the following formula:

$$\text{Degradation ratio (\%)} = \frac{W_0 - W_t}{W_0} \times 100\%$$

#### 4.6 | Mechanical tests

The tensile and compressive tests for film and disc samples were performed on a universal tensile machine (Instron-5967, Canton) with a load cell capacity of 100 N. Rectangular samples with ~0.4 mm in thickness, ~12 mm in length, and ~4 mm in width were cut from the film samples for tensile tests. The constant stretching rate was fixed at 50% min<sup>-1</sup>. In tensile loading-unloading test, the film samples were first loaded to 70% strain and unloaded using the same stretching rate. Successive loading-unloading test was also conducted using increasing applied maximum tensile strains (10%–30%–50%–70% for G, GH, and GHE, while 50%–70%–90%–110%–130%–150% for GHE alone). For compressive tests, hydrogel discs with a diameter of 8 mm and height of 3 mm were employed. A fixed strain rate of 50% min<sup>-1</sup> for uniaxial compressive tests was applied until failure. In compressive loading-unloading test, the disc samples were first loaded to 70% strain and unloaded using the same stretching rate. Successive loading-unloading test was also conducted using increasing applied maximum compressive strains (10%–30%–50%–70% for all groups). For relaxation tests, hydrogel discs were compressed until the strain reached 50%, and samples were allowed to relax for 10 min while maintaining the strain. For anti-fatigue tests, the disc samples were exposed to 100 cycles of ramp force loading and unloading with a constant compressive stress of 20 kPa. The loading and unloading rates were 50% min<sup>-1</sup>. The nominal stress was defined as the applied force divided by the cross-sectional area in the undeformed state. The strain was defined as the elongated sample length divided by the initial length. The modulus was determined by the slope of the stress-strain curve within the 10%–20% strain. The toughness was calculated as integral area of the stress-strain curve. Stress relaxation modulus was measured from the linear slope of the stress relaxation curve over the last 100 s. Elastic recovery was calculated as the ratio between energy of relaxation and the energy of extension.

#### 4.7 | Rheology tests

Rheology experiments were performed on HAAKE MARS Rotational Rheometer with a parallel-plate (P20 TiL, 20 mm

diameter). Apparent viscosities as a function of shear rate (0.1–100 s<sup>-1</sup>) were measured via steady-state flow sweep at a constant temperature of 25°C. Oscillation temperature sweeps were performed over the range from 5°C to 40°C with a heating rate of 2°C min<sup>-1</sup> using an oscillatory frequency of 1 Hz and a shear strain of 1%. Dynamic rheology experiments were exposed to blue light (405 nm, 30 mW cm<sup>2</sup>). Time sweep oscillatory test was performed at a 10% strain (CD mode), 1 Hz frequency, and a 0.5 mm gap for 120 s. The gel point was determined as the time when the storage modulus ( $G'$ ) surpassed the loss modulus ( $G''$ ).

#### 4.8 | Printability tests and morphological analysis of printed constructs

Printability of hydrogels were tested by printing both simple and complex constructs. Printability tests were performed with the 3D-Bioplotter printer (Envision-Tec). For printing simple constructs, all parameters were fixed between groups to compare the printability of different hydrogels, while for printing complex constructs using GHE hydrogel, parameters were adjusted timely to achieve satisfied outcomes.

Morphological analysis was performed according to a published method.<sup>[56]</sup> Briefly, printed complex constructs were collected and scanned by the Quantum GX Micro-Computed Tomography Imaging System (PerkinElmer) to obtain DICOM files, which were then imported into Mimics Medical software (version 21.0, Materialise) for 3D reconstruction to generate standard template library data. Both 3D reconstructed model data and initial digital template data were input into Geomagic Control software (version 2015). The initial digital template data were set as a reference, while the 3D reconstructed model data were set as the test. After fitting and alignment, the morphological similarity of the two models was analyzed by 3D deviation comparison and displayed in the form of a deviation chromatogram.

#### 4.9 | Isolation and cultivation of auricular chondrocytes

Auricular cartilage was obtained from Bama miniature pigs and minced into 1 mm<sup>3</sup> pieces. The cartilage pieces were washed with DPBS and digested with 0.2% COL IV to isolate chondrocytes under gentle agitation at 37°C overnight. Then, the chondrocytes were collected, cultured, and expanded in high glucose DMEM containing 10% fetal bovine serum and 1% PSN at 37°C with 95% humidity and 5% CO<sub>2</sub>. Chondrocytes in the second passage were harvested for further experiments.

#### 4.10 | Cell viability assay, F-actin staining, and immunostaining of COL II

Cell viability was assessed by the live/dead viability/cytotoxicity kit according to the manufacturers' instructions. Briefly, the extruded hydrogel bulks were washed with DPBS, followed by the addition of live/dead staining solution containing 4 mM of calcein acetoxymethyl and 2 mM of ethidium homodimer-1 in DPBS. After incubation at 37°C

for 30 min, the samples were washed and observed under a confocal microscope (Leica TCS SP8 CARS). Percentages of viable cells were determined using the ImageJ software (National Institutes of Health).

For morphological analyses, TRITC-Phalloidin kit was used for 15 min according to the instruction. Briefly, the extruded hydrogel bulks were washed and fixed with 4% (v/v) paraformaldehyde for 30 min. After gentle washing three times, the samples were permeabilized with 0.5% (v/v) Triton X-100 for 5 min at room temperature. Then, TRITC-Phalloidin solution was added to cover samples and incubated for 30 min at room temperature. The samples were washed again and then stained with the DAPI (1:1000 [v/v] in DPBS) for 10 min at room. Finally, the samples were washed and observed under a confocal microscope.

The biofunctionalities of chondrocytes encapsulated hydrogel bulks were further confirmed by immunostaining of the ECM for Col II marker. Briefly, the extruded hydrogel bulks were washed and fixed with 4% (v/v) paraformaldehyde for 30 min. After gentle washing three times, the samples were permeabilized with 0.5% (v/v) Triton X-100 for 5 min and blocked with 5% (v/v) goat serum in PBS for 2 h at room temperature. The samples were then incubated with the desired primary antibody (1:200) overnight at 4°C. The samples were washed and incubated overnight at 4°C with the relevant secondary antibody (Alexa Fluor 488) at 1:200 dilution in blocking buffer. Last, the nuclei were counterstained with DAPI after washing and examined under a confocal microscope. To semi-quantify the expression of Col II marker, fluorescence-based intensity profiles across the central portion were characterized using ImageJ according to the method published.<sup>[57]</sup>

#### 4.11 | Bioprinting and regeneration of elastic cartilage in vivo

The cell-laden hydrogel discs and bioprinted auricle-shaped constructs were implanted hypodermically into mice. The animals were anaesthetized with ketamine and xylazine (35–40 mg kg<sup>-1</sup>, 0.2 mg kg<sup>-1</sup>). All the layers of skin were cut and some pockets were formed through blunt dissection between the dorsal fascia and the panniculus muscle to provide space for the implants. Then, the implants were carefully placed in the space. The incisions were closed layer by layer with 5-0 non-absorbable suture lines. After the operations, analgesics and antibiotics were treated to the experimental animals. The animals were raised until 2 or 3 months later. Then both the animals were sacrificed to explant the samples.

#### 4.12 | Histological, immunohistochemical, and biochemical analysis of explanted tissue

The whole engineering auricular cartilage was used for histological analysis to evaluate the histological structure, proteoglycans, and elastic cartilage-specific ECM deposition in the regenerated tissue. Harvested specimens were fixed in 4% paraformaldehyde overnight at 4°C, embedded in paraffin, and sectioned into 5 μm intervals. The sections were stained based on standard protocols with H&E,

Safranin O, and Victoria blue staining. The expression of COL II and elastin of engineered cartilage was detected by rabbit anti-COL II polyclonal antibody, mouse anti-elastin monoclonal antibody (1:200), and horseradish peroxidase-conjugated anti-mouse antibody (1:200) followed by color development with DAB detection IHC kit.

Specimens ( $n = 3$ ) were collected and minced to conduct cartilage related biochemical evaluations for GAG content and total collagen content. GAG content was determined using the dimethylmethylene blue assay (GenMed Scientifics Inc.), and the total collagen content was detected using the hydroxyproline assay kit (Nanjing Jiancheng Bioengineering Institute). The experiments were conducted according to the manufacturers' instructions.

#### 4.13 | Statistical analysis

Quantitative data were collected from at least three repeated tests and presented as the means ± standard deviation. Following confirmation of a normal distribution of the data, Student's *t*-test or one-way analysis of variance was used to determine the statistical significance using GraphPad Prism 9.3.1 software, and a value of  $p < 0.05$  was considered statistically significant.

#### ACKNOWLEDGMENTS

The authors acknowledge supports by the Chinese Academy of Medical Sciences Innovation Fund for Medical Sciences (2021-I2M-1-052 and 2017-I2M-1-007), the National Multi-disciplinary Cooperative Diagnosis and Treatment Capacity Building Project for Major Diseases (21025), and the National Natural Science Foundation of China (82371796 and 81871575).

#### CONFLICT OF INTEREST STATEMENT

The authors have no competing interests to declare that are relevant to the content of this article.

#### ORCID

Di Wang  <https://orcid.org/0000-0002-8904-2981>

Haiyue Jiang  <https://orcid.org/0009-0003-5838-4828>

#### REFERENCES

1. E. M. Green, J. C. Mansfield, J. S. Bell, C. P. Winlove, *Interface Focus* **2014**, *4*, 20130058.
2. a) D. V. Luquetti, E. Leoncini, P. Mastroiacovo, *Birth Defects Res. A Clin. Mol. Teratol.* **2011**, *91*, 813; b) Y. Zhang, H. Jiang, Q. Yang, L. He, X. Yu, X. Huang, R. Wu, M. Yang, C. Li, B. Pan, *Plast. Reconstr. Surg.* **2018**, *142*, 892e.
3. a) Y. Cao, A. Rodriguez, M. Vacanti, C. Ibarra, C. Arevalo, C. A. Vacanti, *J. Biomater. Sci. Polym. Ed.* **1998**, *9*, 475; b) M. Olausson, P. B. Patil, V. K. Kuna, P. Chougule, N. Hernandez, K. Methe, C. Kullberg-Lindh, H. Borg, H. Ejnell, S. Sumitran-Holgersson, *Lancet* **2012**, *380*, 230; c) G. Zhou, H. Jiang, Z. Yin, Y. Liu, Q. Zhang, C. Zhang, B. Pan, J. Zhou, X. Zhou, H. Sun, D. Li, A. He, Z. Zhang, W. Zhang, W. Liu, Y. Cao, *EBioMedicine* **2018**, *28*, 287.
4. a) Y. S. Zhang, R. Oklu, M. R. Dokmeci, A. Khademhosseini, *Cold Spring Harb. Perspect. Med.* **2018**, *8*, a025718; b) M. Akbari, A. Khademhosseini, *Cell* **2022**, *185*, 2644; c) N. Tan, Y. Y. Yang, *Matter* **2021**, *4*, 2659.
5. a) L. Jia, Y. Hua, J. Zeng, W. Liu, D. Wang, G. Zhou, X. Liu, H. Jiang, *Bioact. Mater.* **2022**, *16*, 66; b) H. Ravanbakhsh, Z. Luo, X. Zhang, S. Maharjan, H. S. Mirkarimi, G. Tang, C. Chávez-Madero, L. Mongeau, Y. S. Zhang, *Matter* **2022**, *5*, 573.

6. a) S. M. Hull, L. G. Brunel, S. C. Heilshorn, *Adv. Mater.* **2022**, *34*, 2103691; b) Y. S. Zhang, A. Khademhosseini, *Science* **2017**, *356*, eaaf3627.
7. H. Ravanbakhsh, G. Bao, Z. Luo, L. G. Mongeau, Y. S. Zhang, *ACS Biomater. Sci. Eng.* **2021**, *7*, 4009.
8. P. Dorishetty, N. K. Dutta, N. R. Choudhury, *Adv. Colloid Interface Sci.* **2020**, *281*, 102163.
9. L. Andrique, G. Recher, K. Alessandri, N. Pujol, M. Feyeux, P. Bon, L. Cognet, P. Nassoy, A. Bikfalvi, *Sci. Adv.* **2019**, *5*, eaau6562.
10. X. Kuang, M. O. Arican, T. Zhou, X. Zhao, Y. S. Zhang, *Acc. Mater. Res.* **2023**, *4*, 101.
11. a) A. P. Dhand, J. H. Galarraga, J. A. Burdick, *Trends Biotechnol.* **2021**, *39*, 519; b) S. Hong, D. Sycks, H. F. Chan, S. Lin, G. P. Lopez, F. Guilak, K. W. Leong, X. Zhao, *Adv. Mater.* **2015**, *27*, 4035; c) K. Cui, J. P. Gong, *Aggregate* **2021**, *2*, e33.
12. J. P. Gong, Y. Katsuyama, T. Kurokawa, Y. Osada, *Adv. Mater.* **2003**, *15*, 1155.
13. J. Kim, G. Zhang, M. Shi, Z. Suo, *Science* **2021**, *374*, 212.
14. D. Xia, J. Chen, Z. Zhang, M. Dong, *Aggregate* **2022**, *3*, e176.
15. D. Wang, S. Maharjan, X. Kuang, Z. Wang, L. S. Mille, M. Tao, P. Yu, X. Cao, L. Lian, L. Lv, J. J. He, G. Tang, H. Yuk, C. K. Ozaki, X. Zhao, Y. S. Zhang, *Sci. Adv.* **2022**, *8*, eabq6900.
16. F. W. Keeley, C. M. Bellingham, K. A. Woodhouse, *Philos. Trans. R Soc. Lond. B Biol. Sci.* **2002**, *357*, 185.
17. a) D. Miranda-Nieves, E. L. Chaikof, *ACS Biomater. Sci. Eng.* **2017**, *3*, 694; b) M. S. Desai, E. Wang, K. Joyner, T. W. Chung, H.-E. Jin, S.-W. Lee, *Biomacromolecules* **2016**, *17*, 2409.
18. Y. Zhang, M. S. Desai, T. Wang, S.-W. Lee, *Biomacromolecules* **2020**, *21*, 1149.
19. a) S. Ito, S. Ishimaru, S. E. Wilson, *Angiology* **1998**, *49*, 289; b) T. Ooyama, K. Fukuda, H. Oda, H. Nakamura, Y. Hikita, *Arteriosclerosis* **1987**, *7*, 593.
20. a) S. G. Wise, G. C. Yeo, M. A. Hiob, J. Rnjak-Kovacina, D. L. Kaplan, M. K. Ng, A. S. Weiss, *Acta Biomater.* **2014**, *10*, 1532; b) Z. Indik, W. R. Abrams, U. Kucich, C. W. Gibson, R. P. Mecham, J. Rosenbloom, *Arch. Biochem. Biophys.* **1990**, *280*, 80.
21. a) N. Annabi, K. Tsang, S. M. Mithieux, M. Nikkhah, A. Ameri, A. Khademhosseini, A. S. Weiss, *Adv. Funct. Mater.* **2013**, *23*, 4950; b) J. Rnjak-Kovacina, S. G. Wise, Z. Li, P. K. Maitz, C. J. Young, Y. Wang, A. S. Weiss, *Biomaterials* **2011**, *32*, 6729; c) S. Lee, E. S. Sani, A. R. Spencer, Y. Guan, A. S. Weiss, N. Annabi, *Adv. Mater.* **2020**, *32*, 2003915.
22. X. Zhao, *Soft Matter* **2014**, *10*, 672.
23. J. P. Gong, *Soft Matter* **2010**, *6*, 2583.
24. a) J. W. Nichol, S. T. Koshy, H. Bae, C. M. Hwang, S. Yamanlar, A. Khademhosseini, *Biomaterials* **2010**, *31*, 5536; b) H. Montazerian, A. Baidya, R. Haghniaz, E. Davoodi, S. Ahadian, N. Annabi, A. Khademhosseini, P. S. Weiss, *ACS Appl. Mater. Interfaces* **2021**, *13*, 40290.
25. a) Y. Hong, F. Zhou, Y. Hua, X. Zhang, C. Ni, D. Pan, Y. Zhang, D. Jiang, L. Yang, Q. Lin, Y. Zou, D. Yu, D. E. Arnot, X. Zou, L. Zhu, S. Zhang, H. Ouyang, *Nat. Commun.* **2019**, *10*, 2060; b) Y. Yang, J. Zhang, Z. Liu, Q. Lin, X. Liu, C. Bao, Y. Wang, L. Zhu, *Adv. Mater.* **2016**, *28*, 2724; c) Y. Hua, H. Xia, L. Jia, J. Zhao, D. Zhao, X. Yan, Y. Zhang, S. Tang, G. Zhou, L. Zhu, Q. Lin, *Sci. Adv.* **2021**, *7*, eabg0628.
26. C. Lu, X. Wang, Y. Shen, C. Wang, J. Wang, Q. Yong, F. Chu, *Adv. Funct. Mater.* **2022**, *32*, 2207714.
27. O. Chaudhuri, L. Gu, D. Klumpers, M. Darnell, S. A. Bencherif, J. C. Weaver, N. Huebsch, H. P. Lee, E. Lippens, G. N. Duda, D. J. Mooney, *Nat. Mater.* **2016**, *15*, 326.
28. a) S. M. Lien, L. Y. Ko, T. J. Huang, *Acta Biomater.* **2009**, *5*, 670; b) F. J. O'Brien, B. A. Harley, M. A. Waller, I. V. Yannas, L. J. Gibson, P. J. Prendergast, *Technol. Health Care* **2007**, *15*, 3.
29. a) D. J. Griffon, M. R. Sedighi, D. V. Schaeffer, J. A. Eurell, A. L. Johnson, *Acta Biomater.* **2006**, *2*, 313; b) L. Zeng, Y. Yao, D. A. Wang, X. Chen, *Mater. Sci. Eng. C Mater. Biol. Appl.* **2014**, *34*, 168.
30. a) N. A. Peppas, J. Z. Hilt, A. Khademhosseini, R. Langer, *Adv. Mater.* **2006**, *18*, 1345; b) J. M. Lee, W. L. Ng, W. Y. Yeong, *Appl. Phys. Rev.* **2019**, *6*, 011307.
31. M. S. Desai, E. Wang, K. Joyner, T. W. Chung, H. E. Jin, S. W. Lee, *Biomacromolecules* **2016**, *17*, 2409.
32. F. J. Verneery, S. Lalitha Sridhar, A. Muralidharan, S. J. Bryant, *Chem. Rev.* **2021**, *121*, 11085.
33. F. Meng, E. M. Terentjev, *Polymers* **2017**, *9*, 52.
34. L. Fu, L. Li, Q. Bian, B. Xue, J. Jin, J. Li, Y. Cao, Q. Jiang, H. Li, *Nature* **2023**, *618*, 740.
35. J. Gosline, M. Lillie, E. Carrington, P. Guerette, C. Ortlepp, K. Savage, *Philos. Trans. R Soc. Lond. B Biol. Sci.* **2002**, *357*, 121.
36. C. A. Hoeve, P. J. Flory, *Biopolymers* **1974**, *13*, 677.
37. J. M. Gosline, *Symp. Soc. Exp. Biol.* **1980**, *34*, 332.
38. K. Dey, S. Agnelli, L. Sartore, *Biomater. Sci.* **2019**, *7*, 836.
39. A. Mongera, M. Pochitaloff, H. J. Gustafson, G. A. Stooke-Vaughan, P. Rowghanian, S. Kim, O. Campàs, *Nat. Mater.* **2023**, *22*, 135.
40. S. Hou, P. X. Ma, *Chem. Mater.* **2015**, *27*, 7627.
41. W. Schuurman, P. A. Levett, M. W. Pot, P. R. van Weeren, W. J. A. Dhert, D. W. Huttmacher, F. P. W. Melchels, T. J. Klein, J. Malda, *Macromol. Biosci.* **2013**, *13*, 551.
42. L. Jiafeng, S. Jiaming, L. Xiaodan, *J. Plast. Reconstr. Aesthet. Surg.* **2016**, *69*, 1430.
43. a) Y. Jin, C. Liu, W. Chai, A. Compaan, Y. Huang, *ACS Appl. Mater. Interfaces* **2017**, *9*, 17456; b) W. Piedra-Cascón, V. R. Krishnamurthy, W. Att, M. Revilla-León, *J. Dent.* **2021**, *109*, 103630.
44. K. L. McCullagh, R. N. Shah, B. Y. Huang, *Neuroimaging Clin. N. Am.* **2022**, *32*, 809.
45. a) C. Gaut, K. Sugaya, *Regen. Med.* **2015**, *10*, 665; b) L. Nimeskern, M. M. Pleumeekers, D. J. Pawson, W. L. Koevoet, I. Lehtoviita, M. B. Soyka, C. Roosli, D. Holzmann, G. J. van Osch, R. Muller, K. S. Stok, *J. Biomech.* **2015**, *48*, 1721.
46. a) T. Takebe, S. Kobayashi, H. Kan, H. Suzuki, Y. Yabuki, M. Mizuno, T. Adegawa, T. Yoshioka, J. Tanaka, J. Maegawa, H. Taniguchi, *Transplant. Proc.* **2012**, *44*, 1158; b) L. García-Martínez, F. Campos, C. Godoy-Guzmán, M. Del Carmen Sánchez-Quevedo, I. Garzón, M. Alaminos, A. Campos, V. Carriel, *Histochem. Cell Biol.* **2017**, *147*, 83.
47. C. Yan, M. E. Mackay, K. Czymmek, R. P. Nagarkar, J. P. Schneider, D. J. Pochan, *Langmuir* **2012**, *28*, 6076.
48. A. C. Hall, *Curr. Rheumatol. Rep.* **2019**, *21*, 38.
49. I. L. Kim, S. Khetan, B. M. Baker, C. S. Chen, J. A. Burdick, *Biomaterials* **2013**, *34*, 5571.
50. a) A. Banerjee, M. Arha, S. Choudhary, R. S. Ashton, S. R. Bhatia, D. V. Schaffer, R. S. Kane, *Biomaterials* **2009**, *30*, 4695; b) H. Hwangbo, H. Lee, E. J. Jin, J. Lee, Y. Jo, D. Ryu, G. Kim, *Bioact. Mater.* **2022**, *8*, 57; c) A. J. Engler, S. Sen, H. L. Sweeney, D. E. Discher, *Cell* **2006**, *126*, 677.
51. a) X. Li, S. Chen, J. Li, X. Wang, J. Zhang, N. Kawazoe, G. Chen, *Polymers* **2016**, *8*, 269; b) W. Liu, M. A. Heinrich, Y. Zhou, A. Akpek, N. Hu, X. Liu, X. Guan, Z. Zhong, X. Jin, A. Khademhosseini, Y. S. Zhang, *Adv. Healthcare Mater.* **2017**, *6*, 1601451.
52. H. J. Yoon, S. R. Shin, J. M. Cha, S. H. Lee, J. H. Kim, J. T. Do, H. Song, H. Bae, *PLoS One* **2016**, *11*, e0163902.
53. S. Khetan, M. Guvendiren, W. R. Legant, D. M. Cohen, C. S. Chen, J. A. Burdick, *Nat. Mater.* **2013**, *12*, 458.
54. T. de Chalain, J. H. Phillips, A. Hinek, *J. Biomed. Mater. Res.* **1999**, *44*, 280.
55. S. M. Partridge, H. F. Davis, G. S. Adair, *Biochem. J.* **1955**, *61*, 11.
56. A. Schwab, R. Levato, M. D'Este, S. Piluso, D. Eglín, J. Malda, *Chem. Rev.* **2020**, *120*, 11028.
57. S. Massa, M. A. Sakr, J. Seo, P. Bandaru, A. Arneri, S. Bersini, E. Zare-Eelanjegh, E. Jalilian, B.-H. Cha, S. Antona, A. Enrico, Y. Gao, S. Hassan, J. P. Acevedo, M. R. Dokmeci, Y. S. Zhang, A. Khademhosseini, S. R. Shin, *Biomicrofluidics* **2017**, *11*, 044109.

## SUPPORTING INFORMATION

Additional supporting information can be found online in the Supporting Information section at the end of this article.

**How to cite this article:** D. Wang, J. Zeng, H. Zhu, S. Liu, L. Jia, W. Liu, Q. Wang, S. Wang, W. Liu, J. Zhou, H. Chen, X. Liu, H. Jiang, *Aggregate* **2024**, e477. <https://doi.org/10.1002/agt2.477>